

Through Lévy Walks to Brownian Walks in the Transport of Filaments in Cellular Flows

Shi-Yuan Hu,^{1,2} Jun-Jun Chu,³ Michael J. Shelley,^{1,4,*} and Jun Zhang^{1,2,5,†}

¹*Applied Mathematics Lab, Courant Institute of Mathematical Sciences,
New York University, New York, NY 10012, USA*

²*Department of Physics, New York University, New York, NY 10003, USA*

³*School of Physics Science and Engineering, Tongji University, Shanghai 200092, China*

⁴*Center for Computational Biology, Flatiron Institute, New York, NY 10010, USA*

⁵*NYU-ECNU Institute of Physics at NYU Shanghai, Shanghai 200062, China*

(Dated: July 23, 2022)

In a spatially periodic and time-independent cellular background flow, flexible filaments can move across closed streamlines and show complex paths and deformations. Here, we study the dynamics of such filaments when their length is long enough to broadly sample the background velocity field. Using simulation, we show that their long-time dynamics evinces various transport states such as Lévy walks, Brownian walks, ballistic transport, and trapping, depending upon the filament's relative length and effective flexibility. In particular, we demonstrate a transition through Lévy walks to Brownian walks with increasing length. Even completely rigid filaments, whose dynamics is finite-dimensional, show a variety of transport states. We find evidence of these various transport states in experiments using arrays of counter-rotating rollers, immersed in a fluid and transporting a flexible ribbon.

Flows in nature are often spatially complex and yet structured. Ocean currents are embedded with counter-rotating eddies, which play important roles in the transport of heat and material [1–4]. At small scale, the flow fields induced by the collective motion of swimming bacteria consists of many coherent vortices and jets [5–9]. The transport, mixing, and pattern formation of suspended particles and filaments in such flows have drawn much interest due to their potential applications to oceanic ecology and bioengineering [10–14]. Different phenomena emerge as the result of the interplay between flows and particles at different length scales.

To capture the essential nonlinear interactions in a simplified setting, idealized cellular flows, namely arrays of counter-rotating vortices, are frequently used. Previous studies on the transport of elongated rigid particles have mainly focused on the regime where the particle length is negligible compared with the vortex size [13, 15–19]. The motion of such a particle is determined by the local flow velocity and its gradient. This has included active particles, where a variety of behaviors are reported including aggregation [16] and Lévy walks [12, 17]. For flexible filaments, which can show complex deformations [20], the coupling between cross-vortex transport and the buckling instability at the flow stagnation points has been a focus [21–23], in particular in relation with Brownian walks. The recent literature on filament dynamics has been reviewed in Ref. [24]. Much of the large-scale transport and dispersal behaviors remains unexplored, especially in the regime where the filament is relatively rigid but its length is comparable to the vortex size. In this regime, the filament can easily extend across vortices, then the filament velocity is determined nonlocally by the widely distributed background flows along the fila-

ment, leading to correlation or decorrelation in the filament velocity itself. One thus expects richer and complex behaviors.

In this Letter, we use experiments and a comprehensive set of numerical simulations to investigate the transport of semi-rigid filaments when their length L is comparable to the vortex size W in an idealized Stokesian cellular flows. In this regime, the dynamics shows similarity to billiards systems [25–27], in which particles undergo elastic collisions with fixed scatterers on a lattice, in the sense that the background vortices can be viewed as ‘soft’ scatterers [27] for the filament. For the first time, we construct a phase diagram showing rich transport states. In particular, we find that there exist a continuous transition through Lévy walks to Brownian walks as L/W is increased. Lévy walks have been found in the dynamics of active elongated particles in cellular flows, but arises there due to particle motility [17]. Quite remarkably, even completely rigid filaments, which are described by only center-of-mass (CoM) position and orientation, show differing random walks and chaotic motion. Complex yet parameter-dependent dispersal patterns emerge due to the interplay of different length scales.

Besides L and W , the dynamics of a flexible filament depends also upon its elastohydrodynamic length $l_e \sim (B/\mu U_0)^{1/3}$ [28], where B is filament rigidity, μ is fluid viscosity, and U_0 is the characteristic flow velocity. The interplay among the three length scales are captured by two dimensionless control parameters: the relative length $\gamma = L/W$ and the effective flexibility $\eta = (L/l_e)^3$. The filament appears to be more ‘flexible’ when η is larger.

Motivating Experiment.—We set up a cellular flow structure by immersing a square 9-by-9 roller array into a tank of pure glycerol (see Fig. 1 and details in sup-

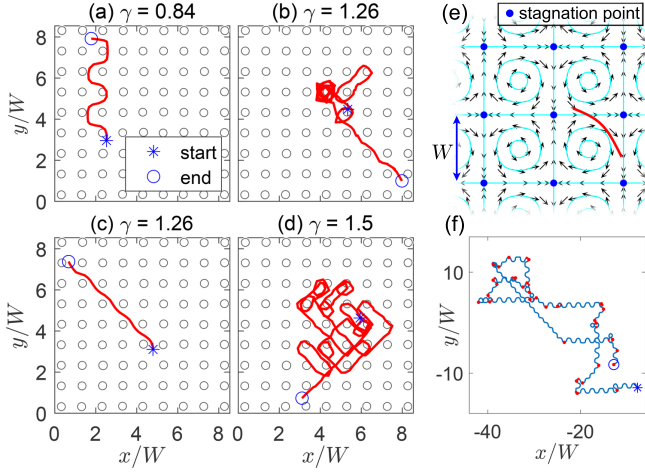


FIG. 1. Experimental CoM trajectories of flexible ribbons in a 9-by-9 cellular flow, as shown on the left. Circles indicate the locations of the spinning rollers. (a) Crenelated step with $\eta \approx 11$. (b) Meandering trajectory with a large zigzag step with $\eta \approx 43$. (c) Zigzag step with $\eta \approx 43$, (d) Meandering trajectory with many turns with $\eta \approx 61$. (e) Snapshot from a numerical simulation with $\eta = 100$ and $\gamma = 1$, showing a flexible filament moving in the cellular flow described by Eq. (1). Black arrows are the background cellular flow and cyan closed curves are the streamlines. (f) A typical trajectory from simulation for $\gamma = 1$ and $\eta = 0.5$ with turning points marked in red.

plemental material [29]). The rollers are interconnected and driven by a stepper motor. Through viscous coupling each roller rotates the fluid around it, with nearest neighbor rollers being counter-rotating. Flexible ribbons, made from audio tape, are transported in the cellular flow and stay right beneath the fluid surface, resembling 2D motions. The Reynolds number $\text{Re} = \rho U_0 W / \mu \approx 0.1 - 1$, where ρ is the density of glycerol. As shown in Fig. 1, a few interesting patterns of ribbon's motion are identified. For moderate γ , despite occasional trappings, the ribbons can reach the edge of the cellular flow through directional zigzag steps along diagonals or directional crenelated steps along the $\pm x$ or $\pm y$ directions [Figs. 1(a), (b), and (c)]. However, for larger γ , the ribbons may meander around for a long time and make many turns before getting to the edge [Fig. 1(d)]. When η is sufficiently large, the ribbons are bent with large deformation and often trapped inside one of the fluid vortices.

Simulation and Model.—We model ribbons as flexible and slender filaments of radius R and length L (with aspect ratio $R/L \ll 1$) moving in a Stokesian flow. Non-dimensionalize space on L , velocity on U_0 , and time on L/U_0 . The background flow \mathbf{U} is given by

$$\mathbf{U} = (\sin(\pi\gamma x) \cos(\pi\gamma y), -\cos(\pi\gamma x) \sin(\pi\gamma y)), \quad (1)$$

with stagnation points at $(n, m)\gamma^{-1}$ for n, m integers. The periodic unit cell is composed of four vortices [Fig. 1(e)]. Parameterize the filament centerline by nor-

malized and centered arclength $s \in [-1/2, 1/2]$ and denote it by $\mathbf{r}(s, t)$, where t is time. From a leading-order slender body approximation [21, 30], the centerline velocity \mathbf{r}_t is governed by a local balance of the drag force with the filament force per unit length upon the fluid,

$$\eta(\mathbf{r}_t - \mathbf{U}[\mathbf{r}]) = (\mathbf{I} + \mathbf{r}_s \mathbf{r}_s)(-\mathbf{r}_{ssss} + (T\mathbf{r}_s)), \quad (2)$$

where η is the effective flexibility and $\mathbf{U}[\mathbf{r}]$ is the background flow distributed along the filament centerline. The filament force is described by Euler-Bernoulli elasticity: $\mathbf{f} = \mathbf{r}_{ssss} - (T\mathbf{r}_s)_s$, where T is the line tension. Substituting Eq. (2) into the inextensibility condition $\mathbf{r}_s \cdot \mathbf{r}_{st} = 0$, we can derive the equation for tension T ,

$$2T_{ss} - \theta_s^2 T = -\eta \mathbf{U}_s \cdot \mathbf{r}_s - 6\theta_{ss}^2 - 7\theta_s \theta_{sss} + \theta_s^4, \quad (3)$$

where θ is the filament tangent angle, and which also satisfies

$$\theta_t = \mathbf{U}_s \cdot \hat{\mathbf{n}} + \eta^{-1}(-\theta_{ssss} + 9\theta_s^2 \theta_{ss} + 3T_s \theta_s + T \theta_{ss}). \quad (4)$$

Equation (2), (3), and (4) are evolved numerically using a second-order finite difference method and implicit time-stepping.

Simulation results.—The filament CoM trajectories have a strong dependence on γ . A common statistical measure of a complex trajectory is its step-length distribution $\phi(l)$ [31]. The step-length l is the straight-line distance between successive turning points [Fig. 1(f)], which are the instants separating the crenelated steps and zigzag steps [29]. For a fixed η and different values of γ , Fig. 2 shows the complement of the cumulative distribution, $C(l) = 1 - \int_a^l \phi(l) dl$, for l in 40 trajectories with several best-fit random walk models using a maximum likelihood method [32, 33]. When $\gamma = 0.7$ [Fig. 2(a)], clusters of short steps are interspersed with long steps between them. The best-fit model is a power law given by $\phi(l) \propto l^{-(1+\beta)}$ indicating Lévy walks [31]. The Lévy exponent $\beta \approx 1.3$. When γ is increased to 1.4 [Fig. 2(c)], the filaments display Brownian walks with homogeneous clusters of small steps within the trajectories. The best-fit model is an exponential distribution. At an intermediate value of γ [Fig. 2(b)], the best-fit model is the Weierstrassian random walk (WRW), which has been found in the studies of animal search strategies and random walks in bacteria swarms [17, 34–36]. The $\phi(l)$ of the WRW is given by a hierarchical weighted sum of exponential distributions: $\phi(l) \propto \sum_{j=0}^J q^{-(j+1)} \lambda^{j+1} \exp(-\lambda^{j+1} l)$, which resembles a power law when $J \rightarrow \infty$ and degenerates into an exponential distribution when $J = 0$. The occurrence of clusters of steps of average size λ^{-j} are q times more likely than clusters of average size $\lambda^{-(j+1)}$. The above transition through Lévy walks to Brownian walks can be confirmed from the scaling of the mean square displacement (MSD) [37], $\langle \delta^2(\tau) \rangle \sim \tau^\nu$ [Fig. 2(d)]. For Lévy walks the scaling exponent $\nu = 3 - \beta$ if $1 < \beta < 2$ [31], and for Brownian walks $\nu = 1$.

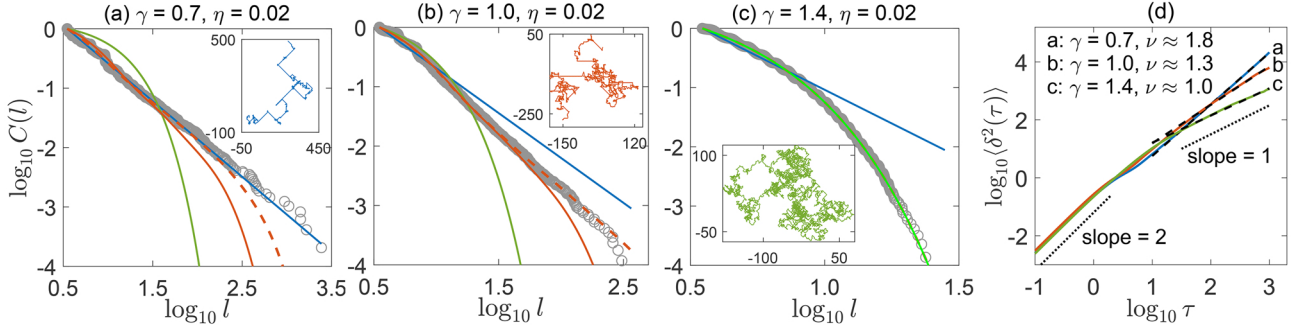


FIG. 2. From Lévy walks to Brownian walks. $C(l)$ at fixed $\eta = 0.02$ for (a) $\gamma = 0.7$, (b) $\gamma = 1$, and (c) $\gamma = 1.4$, with best-fit power law (blue solid lines), 3-tier WRW (red solid line), 5-tier WRW (red dashed line), and exponential distribution (green line). Insets show typical trajectories. (d) MSD $\langle \delta^2(\tau) \rangle$ as a function of τ .

The motion of filaments is chaotic: each individual trajectory depends sensitively on its initial conditions. We compute the time evolution of the Shannon entropy S in phase space starting with an ensemble of random initial conditions [38]. When $\eta \ll 1$, the filament is nearly rigid, and the phase space is approximately three dimensional spanned by the CoM position and the filament orientation (\mathbf{r}_c, θ_c) . For many dynamical systems, after an initial transient regime, the entropy grows linearly and then saturates. The slope of the linear regime is the so-called Kolmogorov-Sinai entropy rate K , which typically equals the sum of the positive Lyapunov exponents [38]. Figure 3(a) shows that K increases when γ is increased, showing that the Brownian walks are more chaotic than Lévy walks.

Mechanism.—We attribute the emergence of chaos and different random walks to the strong nonlocal sampling of the background flow by the filament from its broad extension across vortices. Consider a rigid filament, with centerline $\mathbf{r}(s, t) = \mathbf{r}_c(t) + s\hat{\mathbf{p}}(t)$, with $\hat{\mathbf{p}} = (\cos \theta_c, \sin \theta_c)$ its unit tangent vector. Since the total force upon the filament is zero, the CoM velocity of the filament is $\mathbf{v}_c = (u_c, v_c) = \int_{-1/2}^{1/2} \mathbf{U}[\mathbf{r}(s)] ds$, which is entirely a function of \mathbf{r}_c and θ_c . We first compute the variance of $\mathbf{U}[\mathbf{r}(s)]$: $\text{Var}(\mathbf{U}[\mathbf{r}]) = \langle \int_{-1/2}^{1/2} (\mathbf{U}[\mathbf{r}(s)] - \mathbf{v}_c)^2 ds \rangle$, where the average is taken with respect to \mathbf{r}_c over the entire unit cell and θ_c over $[0, 2\pi)$. With the increase of γ [Fig. 3(b) left], $\text{Var}(\mathbf{U}[\mathbf{r}])$ becomes larger, i.e., the background flow that the filament experienced on average becomes more variable when the filament becomes longer. We also compute the correlation function between the unit velocity vectors of filament's two ends ($s = 1/2, -1/2$): $C_v = \langle \hat{\mathbf{v}}(-1/2) \cdot \hat{\mathbf{v}}(1/2) \rangle$, where the average is along CoM trajectories [Fig. 3(b) right]. When C_v is large, the filament is likely to be translated along a flow but to be turned around when C_v is small. Both $\text{Var}(\mathbf{U}[\mathbf{r}])$ (increasing with γ) and C_v (decreasing with γ) show that long filaments with large γ can hardly travel long unidirectional steps but rather turn around and take seemingly random and diffusive motions. On the other extreme at

very small γ , filaments are too short to perceive any flows outside the local circulation it resides. Therefore, the only possible long-distance travelers are those filaments of intermediate lengths.

Indeed, we find some clues by mapping the spatial distributions of x -component CoM velocity $u_c(\mathbf{r}_c, \theta_c)$. In Figs. 3(c)–3(e), the maps of u_c were made with $\theta_c = 3\pi/4$, but any other values of θ_c in the second and fourth quadrants would result in similar maps but slightly smaller magnitude of u_c . When $\gamma \ll 1$ [Fig. 3(c)], areas of positive u_c values (red, rightward motion) and negative u_c values (blue, leftward motion) are isolated from each other, filament cannot travel across vortices. As γ increases, the red and blue regions start to deform

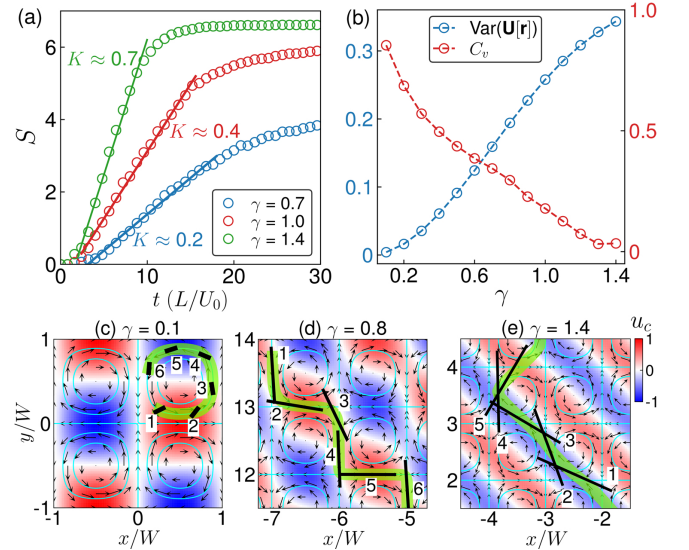


FIG. 3. (a) Shannon entropy S of the phase space evolution for fixed $\eta = 0.02$ and different values of γ . (b) $\text{Var}(\mathbf{U}[\mathbf{r}])$ (left) and C_v (right) as a function of γ . (c), (d), and (e) Maps of positive u_c (red, rightward motion) and negative u_c (blue, leftward motion) computed with $\theta_c = 3\pi/4$ (see text for detail). Snapshots of the motion of rigid filaments are also shown with the time ordering labeled by numbers. Green thick lines trace the CoM trajectories. Black arrows are the background cellular flow and cyan closed curves are the streamlines.

and morph into many alternating ‘conveyor belts’ flowing towards opposite directions [Figs. 3(d), 3(e)]. If θ_c lies in the first and third quadrants, the ‘conveyor belts’ will take the other diagonals oriented $\pi/2$ from those in Figs. 3(d) and 3(e). The filament can now move across vortices and travel long steps. We see two competing effects at work as γ further increases: longer filament promotes the formation of ‘conveyor belts’ but at the same time it is more likely to turn and change directions. The latter effect is demonstrated in Fig. 3(e) as a long filament is captured first by an opposite ‘conveyor belt’ (label 4) and then turns (label 5) with two ends moving oppositely.

The patterns of filament dispersal at scales much larger than W are significantly different for different random walks. For those performing Lévy walks they are strikingly anisotropic. Figure 4(a) shows that for $\gamma = 0.7$, the probability density function (PDF) $P(\mathbf{x}, t)$ of finding a filament at position \mathbf{x} at time t after starting off with random initial conditions from the unit cell centered at the origin has a ‘ \star ’-like structure with four branches extending along the diagonals specified by (\hat{d}_1, \hat{d}_2) . Such anisotropy arises from the long unidirectional zigzag steps along diagonals due to the ‘conveyor belts’. In particular, a sharp peak with a higher density exists at the far front of each branch [Fig. 4(b)] imparting the microscopic geometry of the Lévy walks [39]: filaments can only move along \hat{d}_1 or \hat{d}_2 at each step. If the motions along \hat{d}_1 and \hat{d}_2 are identical and independent 1D Lévy walks, the PDF will be a product of two 1D Lévy distributions [31], $P(d_1, d_2, t) = \mathcal{L}_\beta^\sigma(d_1)\mathcal{L}_\beta^\sigma(d_2)$, where β is the Lévy exponent and the scale parameter $\sigma \propto t^{1/\beta}$. However, if the motions along \hat{d}_1 and \hat{d}_2 are mutually exclusive, then the scale σ of the PDF along $\hat{d}_{2(1)}$ will decrease by a factor of $(1 - d_{1(2)}/(ct))^{1/\beta}$, where c is the average speed of the filaments. Therefore, the PDF along \hat{d}_1 is given by [39],

$$P(d_1, 0, t) = (1 - d_1/(ct))^{-1/\beta} \mathcal{L}_\beta^\sigma(0)\mathcal{L}_\beta^\sigma(d_1), \quad (5)$$

which agrees very well with the simulation result [Fig. 4(b)]. As γ increases, crenelated steps along $\pm x$ or $\pm y$ directions become more frequent and 8-fold ‘ \star ’-like patterns are formed. While almost unapparent, these additional branches can be faintly discerned in Fig. 4(a). Eventually in the Brownian-walk regime for sufficient large γ , in sharp contrast to Lévy walks, the PDF follows an isotropic 2D Gaussian distribution with its variance scaling linearly with time t [40].

By extensively surveying the phase space of γ and η , for the first time, we construct a phase diagram showing various transport states (see Fig. 5(a) and Ref. [29]). Highly flexible filaments ($\eta \gtrsim 10^2$) are deformed and trapped inside vortices for all values of γ , as is also observed in the experiments. For relatively rigid filaments ($\eta \lesssim 10$), the transport states are determined by γ . The boundary that

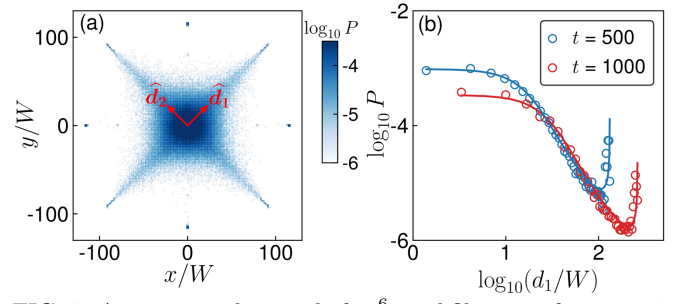


FIG. 4. Anisotropic dispersal of 10^6 rigid filaments for $\gamma = 0.7$ and $\eta \rightarrow 0$. (a) Probability density function (PDF) $P(x, y)$ at $t = 500$. The basis along the diagonals is (\hat{d}_1, \hat{d}_2) . (b) PDF along \hat{d}_1 at two different time instants. Solid lines are the fittings of the theoretical result given by Eq. (5).

separates Lévy walks ($1 < \nu < 2$) and Brownian walks ($\nu \approx 1$) is located around $\gamma = 1.15$. At intermediate η between $10 - 10^2$, the filament first meanders around for a short period before moving unidirectionally and indefinitely along zigzag steps or crenelated steps. We call this type of transport behavior a ballistic state with $\nu \approx 2$. In the ballistic state, filaments with different lengths and flexibility are dynamically sorted due to anisotropic dispersals with strong dependence on both γ and η [29]. The dispersal rate of filaments is largest in ballistic state, followed by Lévy walks and then Brownian walks. There is no long-time transport in the trapping state.

Experimental evidence.—We find evidence that shorter ribbons perform Lévy walks while longer ribbons perform Brownian walks in the experiments [29]. Figures 5(b) and 5(c) show two examples. For $\gamma = 1.26$, the best-fit model is truncated power law (TPL) [41] supporting a Lévy walk; for $\gamma = 1.5$, the step length distribution $C(l)$ better resembles a truncated exponential (TE) model supporting a Brownian walk. The γ value that separates the two

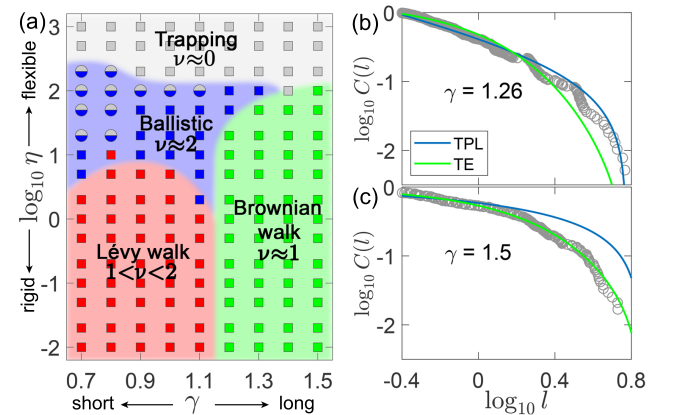


FIG. 5. (a) From simulation, the phase diagram of the transport states classified using MSD and the step length distribution $\phi(l)$ calculated from 100 independent trajectories with random initial conditions. Power-law Lévy walks and WRWs are both classified as Lévy walks. Ballistic state can coexist with trapping state as marked by circles. (b), (c) $C(l)$ from 52 trajectories in experiments for two different values of γ .

states is estimated to be around 1.4, which differs from the value found in the simulation. This discrepancy is possibly caused by the presence of the roller boundaries. Despite the subtle difference in $C(l)$ due to the limited size of the flow field in the experiments, the trajectories for the two states are significantly different from each other as depicted in Fig. 1: with more turns in the trajectories, longer ribbons take much longer time to reach the edge of the flow field than shorter ribbons.

Discussion.—Our experimental and simulation results demonstrate that filaments in cellular flows yield rich dynamics. The emergence of cross-vortex motion and chaos in our system does not require the flow itself to be time-dependent and chaotic as it does for passive pointlike particles [42–45]. Indeed, as $\gamma \rightarrow 0$ the system is Hamiltonian and filaments move along closed orbits within vortices. However, for relatively rigid filaments, those initially near the separatrices between vortices start to escape as γ increases. Eventually, for sufficiently large γ all filaments can move across vortices freely without being trapped, regardless of their initial conditions. For $\gamma \gg 1$ our limited results show mostly Brownian walks, with several seemingly small windows of Lévy walks. Similar to the billiards system [25, 26], the anisotropic dispersals of filaments in the Lévy-walk state and ballistic state are also originated from long unidirectional steps pre-programmed by the fundamental geometries of the backgrounds. However, the dominant directions of motion depend on the relative length γ and effective flexibility η of filaments in our system but are fully specified by the geometries of scatterers in the billiards. Most prominently, various transport states can be achieved by tuning different length scales, which also serves as the underlying mechanism of gel electrophoresis [46]. Our results may open up new possibilities for efficient dynamical sorting of elongated particles and semi-flexible biopolymers [46–51].

We thank L. Ristroph, Y.-N. Young, and J.-Q. Zhong for inspiring questions and helpful discussions. We gratefully acknowledge the MacCracken Fellowship provided by New York University Graduate School of Arts and Science. M. J. Shelley and J. Zhang acknowledge support from National Science Grant CBET-1805506.

* shelley@cims.nyu.edu

† jun@cims.nyu.edu

- [1] M. Lévy, P. J. S. Franks, and K. Shafer Smith, *Nat. Commun.* **9**, 1-16 (2018).
- [2] P.-Y. Le Traon and R. Morrow, *Int. Geophys.* **69**, 171-xi (2001).
- [3] J. C. McWilliams, *Proc. R. Soc. A* **472**, 20160117 (2016).
- [4] S. Rahmstorf, *Nature* **421**, 699 (2003).
- [5] C. Dombrowski *et al.*, *Phys. Rev. Lett.* **93**, 098103 (2004).
- [6] L. H. Cisneros *et al.*, *Exp Fluids* **43**, 737–753 (2007).
- [7] H. P. Zhang *et al.*, *Europhys. Lett.* **87**, 48011 (2009).
- [8] A. Sokolov and I. S. Aranson, *Phys. Rev. Lett.* **109**, 248109 (2012).
- [9] J. Dunkel *et al.*, *Phys. Rev. Lett.* **110**, 228102 (2013).
- [10] A. Sokolov and I. S. Aranson, *Phys. Rev. Lett.* **103**, 148101 (2009).
- [11] X. Wu and A. Libchaber, *Phys. Rev. Lett.* **84**, 3017-3020 (2000).
- [12] G. Ariel *et al.*, *Nat. Commun.* **8**, 8396 (2015).
- [13] W. Clifton and R. N. Bearon, *IMA J. Appl. Math.* **83**, 743–766 (2018).
- [14] A. Provenzale, *Annu. Rev. Fluid Mech.* **31**, 55–93 (1999).
- [15] H. Shin and M. R. Maxey, *Phys. Rev. E* **56**, 5431 (1997).
- [16] C. Torney and Z. Neufeld, *Phys. Rev. Lett.* **99**, 078101 (2007).
- [17] G. Ariel, A. Be’er, and A. Reynolds, *Phys. Rev. Lett.* **118**, 228102 (2017).
- [18] G. Ariel, J. Schiff, *Physica D* **411**, 132584 (2020).
- [19] S. A. Berman, K. A. Mitchell, *Chaos* **30**, 063121 (2020).
- [20] J. LaGrone, R. Cortez, W. Yan, and L. Fauci, *J. Non-newton Fluid Mech.* **269**, 73-81 (2019).
- [21] Y.-N. Young and M. J. Shelley, *Phys. Rev. Lett.* **99**, 058303 (2007).
- [22] E. Wandersman, N. Quennou, M. Fermigier, A. Lindner, and O. du Roure, *Soft matter* **6**, 5715-5719 (2010).
- [23] N. Quennou, M. Shelley, O. du Roure, and A. Lindner, *J. Fluid Mech.* **769**, 387-402 (2015).
- [24] O. du Roure, A. Lindner, E. Nazockdast, and M. J. Shelley, *Annu. Rev. Fluid Mech.* **51**, 539-572 (2019).
- [25] L. Zarfaty *et al.*, *Phys. Rev. E* **98**, 010101(R) (2018).
- [26] L. Zarfaty, A. Peletskyi, E. Barkai, and S. Denisov, *Phys. Rev. E* **100**, 042140 (2019).
- [27] R. Klages *et al.*, *Phys. Rev. Lett.* **122**, 064102 (2019).
- [28] C. H. Wiggins and R. E. Goldstein, *Phys. Rev. Lett.* **80**, 3879 (1998).
- [29] See Supplemental Material for videos showing the motion of filaments in different states, experimental details, step length analysis, and dispersal patterns in ballistic state.
- [30] G. Batchelor, *J. Fluid Mech.* **44**, 419-440 (1970).
- [31] V. Zaburdaev, S. Denisov, and J. Klafter, *Rev. Mod. Phys.* **87**, 483 (2015).
- [32] A. Edwards *et al.*, *Nature* **449**, 1044–1048 (2007).
- [33] A. Clauset, C. R. Shalizi, and M. E. J. Newman, *SIAM Rev.* **51**, 661-703 (2009).
- [34] A. M. Reynolds, P. Schultheiss, and K. Cheng, *J. Theor. Biol.* **340**, 17-22 (2014).
- [35] A. M. Reynolds, *Sci. Rep.* **4**, 4409 (2014).
- [36] B. D. Hughes, M. F. Shlesinger, and E. W. Montroll, *Proc. Natl. Acad. Sci. U.S.A.* **78**, 3287-3291 (1981).
- [37] R. Metzler, J.-H. Jeon, A. G. Cherstvy, and E. Barkai, *Phys. Chem. Chem. Phys.* **16**, 24128 (2014).
- [38] V. Latora and M. Baranger, *Phys. Rev. Lett.* **82**, 520 (1999).
- [39] V. Zaburdaev, I. Fouxon, S. Denisov, and E. Barkai, *Phys. Rev. Lett.* **117**, 270601 (2016).
- [40] S.-Y. Hu, M. J. Shelley, and J. Zhang, in preparation.
- [41] D. A. Raichlen *et al.*, *Proc. Natl. Acad. Sci. U.S.A.* **111**, 728-733 (2014).
- [42] T. H. Solomon, E. R. Weeks, and H. L. Swinney, *Phys. Rev. Lett.* **71**, 3975 (1993).
- [43] T. H. Solomon and J. P. Gollub, *Phys. Rev. A* **38**, 6280 (1998).
- [44] N. Khurana, J. Blawdziewicz, and N. T. Ouellette, *Phys.*

- Rev. Lett. **106**, 198104 (2011).
- [45] R. Festa, A. Mazzino, and M. Todini, Phys. Rev. E **80**, 035301 (R) (2009).
 - [46] K. D. Dorfman *et al.*, Chem. Rev. **113**, 2584-2667 (2013).
 - [47] B. Chakrabarti, C. Gaillard, and D. Saintillan, Soft Matter **16**, 5534-5544 (2020).
 - [48] L. R. Huang *et al.*, Nat. Biotechnol. **20**, 1048-1051 (2002).
 - [49] A. Oudenaarden and S. G. Boxer, Science **285**, 1046-1048 (1999).
 - [50] J. Shin, A. G. Cherstvy, W. K. Kim, and V. Zaburdaev, Phys. Chem. Chem. Phys. **19**, 18338-18347 (2017).
 - [51] P. Sajeesh and A. K. Sen, Microfluid Nanofluid **17**, 1-52 (2014).

Supplemental Material for Through Lévy Walks to Brownian Walks in the Transport of Filaments in Cellular Flows

Shiyuan Hu,^{1,2} Junjun Chu,³ Michael Shelley,^{1,4,*} and Jun Zhang^{1,2,5,†}

¹*Applied Mathematics Lab, Courant Institute of Mathematical Sciences,
New York University, New York, NY 10012, USA*

²*Department of Physics, New York University, New York, NY 10003, USA*

³*School of Physics Science and Engineering, Tongji University, Shanghai 200092, China*

⁴*Center for Computational Biology, Flatiron Institute, New York, NY 10010, USA*

⁵*New York University-East China Normal University Institute of Physics,
New York University Shanghai, Shanghai 200062, China*

(Dated: July 23, 2022)

VIDEO INFORMATION

Video1 (simulation): Filament in trapping state with $\gamma = 1.2$ and $\eta = 1000$.

Video2 (simulation): Filament in Ballistic state taking crenelated step with $\gamma = 1$ and $\eta = 50$.

Video3 (simulation): Filament in Ballistic state taking zigzag step with $\gamma = 1.2$ and $\eta = 50$.

Video4 (simulation): Filament in Lévy-walk state with $\gamma = 0.9$ and $\eta = 0.1$.

Video5 (simulation): Filament in Brownian-walk state with $\gamma = 1.4$ and $\eta = 0.5$.

Video6 (experiment): Directional motion of ribbon with $\gamma = 1.26$ and $\eta \approx 43$. (Trajectory Duration 30.5 sec.)

Video7 (experiment): Meandering motion of ribbon with $\gamma = 1.5$ and $\eta \approx 61$. (Trajectory Duration 204 sec.)

Occasionally, the experimental center-of-mass (CoM) trajectory lacks smoothness. This is largely due to the imperfect tracking caused by the extremely thin ribbon. When our tracking algorithm processes the video recordings (with a broad view field), it fails at times to recognize the entire filament.

EXPERIMENTAL DETAILS

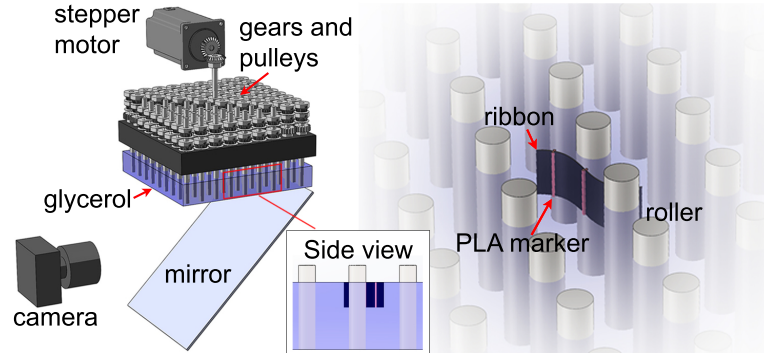


FIG. 1. Schematic of the experimental setup as shown on the left. Right panel details a ribbon moving between rollers.

The experiment setup is shown in Fig. 1. We immerse a square 9-by-9 roller array into a tank of pure glycerol from the above. The fluid surface is free and its bottom is no-slip. The center-to-center distance between the nearest neighbor rollers is $W = 19$ mm, and the diameter of the roller is 6.35 mm. Other parameters are listed in Table I. The rollers are inter-connected with gears, pulleys, and timing belts and driven by a stepper motor, such that nearest neighbor rollers are counter-rotating and rollers in the same diagonal are co-rotating. Each roller rotates the fluid around it through viscous coupling and a cellular flow structure is formed. Different from our method, another way to form cellular flows is using electromagnetic forcing [1].

In our experiments, we transport flexible ribbons made from audio tapes that are slightly denser than glycerol. To prevent the ribbon from sinking, we attach equally-spaced PLA markers, thin rods of 1 mm diameter, to the ribbon

because PLA is lighter than glycerol. As a result, the ribbon stays right beneath the free surface and remains vertical due to the quasi-2D flow. Since the ribbon width is small compared with the depth of the fluid, we can neglect the effect of the no-slip bottom of the tank on ribbon's motion. Therefore, the motion of the ribbon is essentially 2D. The PLA markers can also make the video tracking easier. The motion of the ribbon is recorded by a camera through a reflection mirror at 45° with respect to the horizontal plane. We then process the video using Matlab Image Processing Toolbox and obtain the CoM trajectories.

In the experiment, the two control parameters are the rotation frequency f_0 of the stepper motor and the ribbon length L . We vary f_0 between 0.3 Hz and 1.5 Hz and experiment on three values of L : 16 mm, 24 mm, and 28.5 mm. The effective flexibility η can be estimated. For example, when $L = 24$ mm and $f_0 = 1$ Hz,

$$\eta = \left(\frac{L}{l_e}\right)^3 \sim \frac{\mu U_0 L^3}{B} = \frac{\mu f_0 L^4}{B} \approx 62, \quad (1)$$

where μ is the dynamical viscosity of glycerol and the characteristic flow velocity $U_0 = f_0 L$.

Geometric parameters	
distance of neighbor rollers W	19 mm
roller diameters	6.35 mm
fluid depth	25 mm
tank size	171 mm×171 mm×30 mm
Material parameters	
ribbon width	6×10^{-3} m
ribbon thickness	2.54×10^{-5} m
ribbon bending rigidity B	7.6×10^{-9} J·m
ribbon density	$1.3\text{--}1.4 \times 10^3$ kg/m ³
glycerol density	1.26×10^3 kg/m ³
glycerol dynamic viscosity, μ	1.412 Pa·s
PLA density	1.24×10^3 kg/m ³
diameter of PLA marker	1×10^{-3} m

TABLE I. Parameters of the experimental setup.

	η	Distribution	Akaike weights w
$\gamma = 0.84$	12	truncated exponential	0.05
		truncated power law	0.95
$\gamma = 1.26$	18	truncated exponential	0
		truncated power law	1
	43	truncated exponential	0
		truncated power law	1
$\gamma = 1.50$	57	truncated exponential	0.04
		truncated power law	0.96
	61	truncated exponential	1
		truncated power	0
$\gamma = 1.50$	86	truncated power law	1
		truncated power law	0

TABLE II. From experiments, Akaike weights of best-fit truncated power law and truncated exponential distribution for $\gamma = 0.82, 1.26$, and 1.5 with different values of η .

STEP-LENGTH DISTRIBUTION ANALYSIS

The step length l is the straight-line distance between successive turning points separating the zigzag steps and crenelated steps. To identify the turning points, we first find the local minimums and maximums of the x coordinate of the CoM trajectories [Fig. 2], and then calculate the straight-line distances between each two neighbor extremums. If a distance is smaller than a minimum value l_{\min} , we discard the corresponding leading extremum used in computing

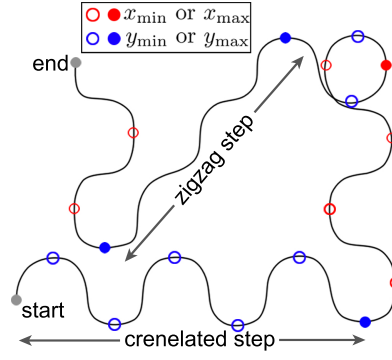


FIG. 2. Determination of the turning points by finding the local minimums and maximums of the x and y coordinates of the CoM trajectory. The red circles are the extremums of x coordinates and the blue circles are the extremums of y coordinates. Open circles are discarded and filled circles are determined turning points (including the start and end points).

that distance. The same procedure is repeated for y coordinates. The turning points are the aggregate of the remaining extremums of x and y coordinates while keeping their time ordering. We take l_{\min} to be slightly larger than the vortex size W .

After we obtain the step-length data, we fit it to the candidate distributions mentioned in the main text using a maximum likelihood method [2–4]. The Akaike weight w is then calculated for model selection [5]. The data completely supports the distribution when $w = 1$ and does not support the distribution when $w = 0$. The above approach is robust for identifying Lévy-walk patterns.

In the experiments, since the flow field is bounded, we fit the step-length data to the truncated power law and truncated exponential distribution. The Akaike weights for $\gamma = 0.82, 1.26$ and 1.5 with different values of η are shown in Table II. The step-length data for short filaments ($\gamma = 0.82$ and 1.26) better supports truncated power law. For longer filament ($\gamma = 1.5$), the step-length data better supports truncated exponential distribution.

DYNAMICAL SORTING IN THE BALLISTIC STATE

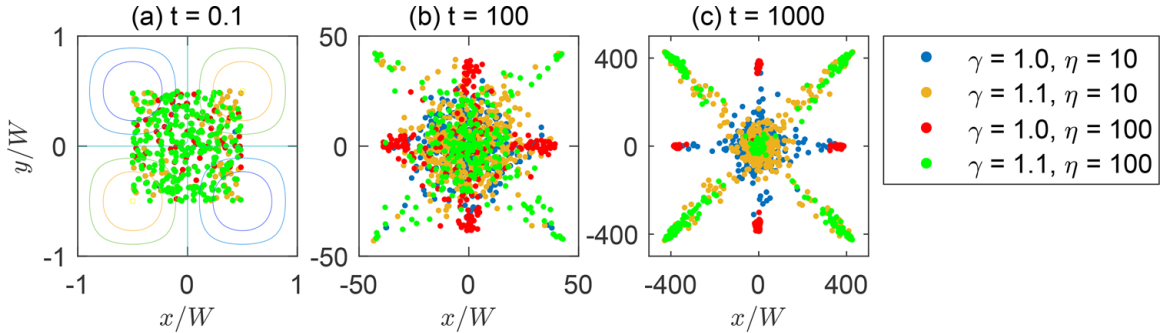


FIG. 3. From simulation, anisotropic dispersals in ballistic state showing the distribution of the CoM positions for four different filament lengths and flexibility: $\gamma = 1, \eta = 10$ (blue), $\gamma = 1.1, \eta = 10$ (yellow), $\gamma = 1, \eta = 100$ (red), and $\gamma = 1.1, \eta = 100$ (green), at (a) $t = 0.1$, (b) $t = 100$, and (c) $t = 1000$.

In the ballistic state, the filament typically meanders around for a short period t_m before taking unidirectional crenelated steps along $\pm x$ and $\pm y$ directions or unidirectional zigzag steps along diagonals. Longer filaments ($\gamma > 1$) are transported along diagonals and shorter filaments ($\gamma \leq 1$) are transported along $\pm x$ and $\pm y$ directions. The dispersals of filaments is anisotropic and depend strongly on γ and η [Fig. 3]. Initially [Fig. 3(a)], four different filaments with different values of γ and η are distributed inside a square region ($x \in [-W/2, W/2]$, $y \in [-W/2, W/2]$) with random initial positions and orientations. The anisotropy in the dispersal patterns grows quickly. When $t = 100$ [Fig. 3(b)], some of the green ($\gamma = 1.1, \eta = 100$) and red filaments ($\gamma = 1, \eta = 100$) are already separated spatially with the green filaments moving along diagonals and red filaments moving along $\pm x$ and $\pm y$ directions. When t is sufficiently large [Fig. 3(c)], four kinds of filaments are already well separated from each other. Filaments with

larger η mainly occupy the dispersal fronts, and filaments with smaller η are distributed along diagonals or x and y directions, i.e., the meandering time t_m decreases as η increases. However, filaments with sufficiently large η will result in trapping state, in which filaments are bent with large deformation and trapped inside one of the vortices.



* shelley@cims.nyu.edu

† jun@cims.nyu.edu

- [1] E. Wandersman, N. Quennou, M. Fermigier, A. Lindner, and O. du Roure, *Soft matter* **6**, 5715-5719 (2010).
- [2] D. A. Raichlen *et al.*, *Proc. Natl. Acad. Sci. U.S.A.* **111**, 728-733 (2014).
- [3] A. Clauset, C. R. Shalizi, and M. Newman, *SIAM Rev.* **51**, 661–703 (2009).
- [4] A. Edwards *et al.*, *Nature* **449**, 1044–1048 (2007).
- [5] K. P. Burnham and D. R. Anderson., *Model selection and multimodel inference: A practical information-theoretic approach*, Springer-Verlag, New York, USA, (2002).